Degree Project in Materials and Process Design

Second Cycle, 30 credits

From Dynamical Instabilities to Structural Disorder: A First Principles Analysis of Lattice Dynamics and Ion Transport in Antiperovskite Electrolytes

TZU-YU SHIH

TRITA-ITM-EX 2026:200
Stockholm, Sweden 2026

www.kth.se

Abstract

Developing safe, high-performance batteries is critical for sustainable energy systems. All-solid-state batteries offer a great solution to both requirements, provided high performance solid electrolytes are developed. Antiperovskite solid electrolytes are promising candidates due to their superionic conductivity, broad electrochemical stability, and compatibility with metallic lithium anodes. However, optimizing their macroscopic ionic transport requires a deep understanding of the thermodynamically dominant metal-halide Schottky defects. This study systematically investigates the influence of these localized defect clusters on ionic transport across six antiperovskite compounds: Li_3OCl, Li_3SCl, Li_3OF, Na_3OCl, Na_3SCl, and Na_3OF. Using Density Functional Theory (DFT) and the climbing image nudged elastic band (CI-NEB) method, we evaluated the migration energy barriers of alkali vacancies. Fluoride-substituted compounds exhibited the most kinetically favorable pathways, with Li_3OF and Na_3OF yielding the lowest barriers (both are 0.21 eV). Conversely, other compositions face distinct structural limitations that significantly increase activation energies; the prototypical Li_3OCl (0.34 eV) is constrained by a highly rigid lattice, while the softer Na_3SCl (0.34 eV) is hindered by an extended migration path distance. Analysis revealed that migration barriers correlate strongly with the Continuous Symmetry Measure (CSM) at the transition state. Ultimately, greater localized lattice distortion, quantified by a higher CSM, fundamentally lowers the migration barrier. By correlating these structural perturbations with local activation energies, this study proposes critical geometric design principles for optimizing defect-driven conduction in next-generation solid-state batteries.

Keywords: All-solid-state batteries; Antiperovskite solid electrolytes; Density Functional Theory (DFT); Nudged Elastic Band (CI-NEB); Schottky defects

Sammanfattning

Att utveckla säkra och högpresterande batterier är avgörande för hållbara energisystem. Solid-state-batterier utgör en utmärkt lösning på båda dessa krav, förutsatt att högpresterande fasta elektrolyter kan utvecklas. Fasta elektrolyter av antiperovskit-typ är lovande kandidater på grund av deras superjoniska ledningsförmåga, breda elektrokemiska stabilitet och kompatibilitet med metalliska litiumanoder. För att optimera deras makroskopiska jontransport krävs dock en djup förståelse av de termodynamiskt dominerande metall-halid-Schottky-defekterna. Denna studie undersöker systematiskt hur dessa lokaliserade defektkluster påverkar jontransporten i sex antiperovskitföreningar: Li_3OCl, Li_3SCl, Li_3OF, Na_3OCl, Na_3SCl, and Na_3OF. Med hjälp av täthetsfunktionalteori (DFT) och metoden climbing image nudged elastic band (CI-NEB) utvärderade vi migrationsenergibarriärerna för alkalimetallvakanser. Fluoridsubstituerade föreningar uppvisade de mest kinetiskt gynnsamma migrationsvägarna, där Li_3OF och Na_3OF gav de lägsta barriärerna (båda på 0,21 eV). Omvänt möter andra sammansättningar distinkta strukturella begränsningar som avsevärt ökar aktiveringsenergierna; den prototypiska Li_3OCl (0,34 eV) begränsas av ett mycket styvt gitter, medan den mjukare Na_3SCl (0,34 eV) hindras av ett förlängt migrationsavstånd. Analysen visade att migrationsbarriärerna korrelerar starkt med ett kontinuerligt symmetrimått (Continuous Symmetry Measure, CSM) vid övergångstillståndet. I slutändan sänker en större lokal gitterförvrängning, kvantifierad genom ett högre CSM, migrationsbarriären fundamentalt. Genom att korrelera dessa strukturella störningar med lokala aktiveringsenergier, föreslår denna studie kritiska geometriska designprinciper för att optimera defektdriven ledning i nästa generations solid-state-batterier.

Nyckelord: Solid-state-batterier; Fasta elektrolyter av antiperovskit-typ; Täthetsfunktionalteori (DFT); Nudged Elastic Band (CI-NEB); Schottky-defekter.

Table of Contents

Abstract I
Sammanfattning II
1. Introduction 1
2. Background 2
2.1. Overview of Solid-State Electrolytes 2
2.2. Antiperovskite Solid Electrolytes 2
2.3. Defect Chemistry and Ionic Transport Mechanisms 3
2.4. Computational Modeling: DFT and CI-NEB 5
2.5. Knowledge Gap and Motivation 6
3. Methodology 7
4. Results and Discussion 8
4.1. Sustainability 15
5. Conclusion 16
6. Future Work 17
Declaration of Generative AI in the Writing Process 17
References 18

1. Introduction

Energy serves as the foundation of modern civilization and is indispensable for economic development, technological advancement, and human welfare. The global economy has experienced unprecedented growth over the past century, with gross domestic product nearly doubling from 11.34 trillion to 25.41 trillion dollars, fundamentally dependent upon reliable and abundant energy supply[1]. However, this energy security has been rooted in non-renewable energy, which currently account for approximately 80% of global energy consumption. This heavy reliance on coal, oil, and natural gas has driven prosperity but at a profound environmental cost: global CO_2 emissions have increased by over 2 times from 1965 to 2022. These emissions have elevated atmospheric CO_2 concentrations to levels over 40% higher than pre-industrial levels, directly driving climate change by rising global temperatures, intensifying heat waves, increasing drought severity, and accelerated extreme weather events[2]. The urgency of transitioning from fossil fuel dependency to sustainable, low-carbon energy sources is now scientifically irrefutable. Therefore, development of efficient, scalable energy storage technologies will be critical to its sustainable utilization.

The electrification of global energy systems and the integration of intermittent renewable sources demand diverse approaches to energy storage that can decouple electricity generation from consumption across multiple timescales. Energy storage technologies span four primary categories with distinct operational principles. Mechanical storage systems (pumped hydroelectric, compressed air, gravity storage) exploit gravitational or compressed energy with high efficiency but require specific geographical features[3, 4]. Thermal storage systems (molten salt, phase-change materials) excel in solar-thermal and industrial applications but lack rapid electricity dispatch capability[4, 5]. Chemical and hydrogen storage convert excess electricity into storable hydrogen through electrolysis, enabling long-duration storage with minimal self-discharge, though round-trip efficiency and infrastructure remain challenging[4]. Electrochemical storage, primarily lithium-ion batteries (LiBs), directly converts electrical to chemical energy through reversible ion transport, offering rapid response, high power density[6].

Among the means of energy storage, LiBs have been a dominant choice in the field of portable devices due to their high energy density, low diffusion barrier, and low-volume expansion[6]. Despite the excellent properties of LiBs, its potential safety risk can limit its application[7]. All-solid-state batteries (ASSBs) utilize non-flammable solid electrolytes to replace conventional liquid electrolytes, effectively mitigating safety risks. An ASSB consists of three components arranged in a stacked, solid-solid configuration: the cathode, the solid electrolyte separator, and the anode. During discharge, chemical reactions within the cathode material release lithium ions, which migrate through the solid electrolyte toward the anode, while electrons simultaneously flow through the external circuit to power an external load. This coupled ionic and electronic transport constitutes the electrochemical cell operation. Unlike conventional LiBs that employ graphite anodes with relatively low volumetric energy density, ASSB designs incorporate lithium metal anodes that exploit lithium's exceptional specific capacity of 3,860 mAh/g and low reduction potential of -3.04 V versus the standard hydrogen electrode, enabling substantially higher energy density than graphite-based systems[6, 7]. Utilizing solid electrolytes can also increase the thermal runaway threshold, thereby preventing detrimental chemical reactions[8]. The reduced production of combustible gases and the lower, slower heat release of ASSBs significantly mitigate both the likelihood and severity of thermal runaway propagation. This material substitution makes ASSBs a safer alternative to traditional LiBs while maintaining high energy density[8].

2. Background

2.1. Overview of Solid-State Electrolytes

In an all-solid-state battery (ASSB), the solid electrolyte functions dually as the ion-conducting medium and the physical separator between electrodes[9]. To perform this role effectively, a viable solid electrolyte must exhibit a high room-temperature ionic conductivity, typically exceeding 10^{-4} S/cm, to facilitate efficient energy transfer[10]. Concurrently, it must maintain negligible electronic conductivity to prevent self-discharge and possess a broad electrochemical stability window to avoid degradation under standard operating voltages.

Historically, the pursuit of optimal solid ionic conductors has spanned from early flexible solid polymers, such as polyethylene oxide (PEO), to diverse inorganic ceramic families. Each established material class, however, presents inherent operational trade-offs. Polymer electrolytes are highly valued for their mechanical flexibility, low flammability, and ability to form compliant interfacial contacts[11]; yet, they are fundamentally limited by low room-temperature ionic conductivities, ranging from 10^{-6} to 10^{-7} S/cm, and narrow electrochemical stability windows[12, 13]. Conversely, oxide-based electrolytes, including the garnet, NASICON, and perovskite families, offer robust chemical stability and high mechanical strength that theoretically suppress lithium dendrite growth[14, 15]. Despite these advantages, oxides are intrinsically brittle, require high sintering temperatures exceeding 1000 °C, and suffer from elevated interfacial resistance due to their structural rigidity, which prevents conformal electrode contact[16]. Alternatively, sulfide solid electrolytes provide exceptional room-temperature ionic conductivities of 10^{-3} to 10^{-2} S/cm and high malleability for dense, low-resistance interfaces[17, 18]. However, they are severely hindered by poor oxidation stability and extreme environmental sensitivity, reacting readily with atmospheric moisture to degrade and release toxic gases[19, 20].

These systemic limitations across traditional polymer, oxide, and sulfide frameworks have catalyzed a distinct transition toward halide and antiperovskite solid electrolytes. Halides, characterized by the general formula Li_3MX_6, benefit from the weaker Coulombic interactions of monovalent halogens, which facilitate rapid ion transport while affording greater oxidative stability than their sulfide counterparts[21, 22]. Building upon these advantageous halogen chemistries, antiperovskite electrolytes have emerged as highly promising alternatives. Defined by a structural inversion from the traditional perovskite ($A^+B^{2+}X_3^-$) to an $A^-B^{2-}X_3^+$ framework, lithium-rich antiperovskites feature a dodecahedral A-site occupied by a halogen anion, an octahedral B-site containing an oxygen anion, and an X-site populated by electropositive lithium cations[23]. This unique crystallographic architecture establishes three-dimensional conducting pathways that enable superionic conductivities exceeding 10^{-3} S/cm at room temperature, coupled with exceptionally low activation energies of 0.2 to 0.3 eV. Furthermore, antiperovskites deliver a broad electrochemical stability window greater than 6 V, exceptional chemical compatibility with metallic lithium anodes, low toxicity, and a lightweight, cost-effective composition[24].

2.2. Antiperovskite Solid Electrolytes

Since the initial design of the room-temperature lithium-ion conducting antiperovskite Li_3OCl by Zhao et al. in 2012[23], the field has rapidly expanded to include various elemental substitutions and doping strategies—such as divalent-cation doping and the incorporation of

mixed chalcogen sublattices—aimed at maximizing ionic mobility to record levels exceeding 10^{-2} S/cm[25-27]. Beyond these kinetic enhancements, antiperovskite solid electrolytes exhibit a suite of compelling electrochemical properties, most notably a broad electrochemical stability window often exceeding 6 V and exceptional compatibility with metallic lithium anodes[28]. This inherent resistance to reduction stems from the constituent cations and anions already existing in their lowest valence states[29]. Furthermore, these materials act as robust electronic insulators; prototypical Li_3OCl, for instance, exhibits a substantial electronic band gap of approximately 6.26 eV, which is a critical feature for effectively suppressing lithium dendrite propagation[28].

Despite their compelling advantages, the widespread deployment of antiperovskite solid electrolytes is hindered by several formidable challenges. A primary practical limitation is their extreme hygroscopicity, which necessitates rigorous handling within stringently controlled inert environments[30, 31]. More fundamentally, the prototypical Li_3OCl phase exhibits thermodynamic metastability at ambient temperatures[29]. Although it can be entropically stabilized under elevated thermal conditions, the lattice remains highly susceptible to phase separation into its constituent binary precursors (Li_2O and LiCl) upon cooling, requiring mitigation strategies such as rapid thermal quenching or compositional tuning for structural preservation[32]. Mechanically, antiperovskites are intrinsically brittle due to a characteristically low bulk-to-shear modulus ratio, rendering them vulnerable to mechanical fracture induced by volumetric fluctuations during extended battery cycling[28, 33]. Additionally, macroscopic ion transport is frequently obstructed by grain boundary resistance, where the localized trapping of charge carriers depletes the bulk lattice and severely attenuates the effective diffusion coefficient[34].

To overcome these kinetic and structural limitations, particularly optimizing ionic conductivity, the focus must shift away from the ideal crystal lattice. A perfect, stoichiometric antiperovskite framework inherently acts as a poor ionic conductor, given that all available lithium sites are fully occupied and tightly coordinated within the octahedral sub-lattice. Consequently, realizing the superionic potential of these electrolytes is fundamentally dependent on the deliberate introduction and manipulation of atomic-level imperfections, thereby establishing the critical imperative for investigating their defect chemistry.

2.3. Defect Chemistry and Ionic Transport Mechanisms

The generation of intrinsic charge carriers in pristine antiperovskites is governed by thermal excitation. First-principles calculations indicate that Frenkel defect formation (the creation of vacancy-interstitial pairs) is energetically demanding; for instance, the formation energy in Li_3OCl is calculated to be approximately 1.94 to 2.02 eV, resulting in negligible interstitial concentrations at ambient temperatures[35]. Conversely, LiCl Schottky defects exhibit significantly lower formation energies and are thermodynamically favored. The prevalent formation of metal-halide Schottky defects, such as the stoichiometric removal of a LiCl unit yielding a lithium vacancy (V'_{Li}) and a chlorine vacancy ($V^{\cdot}_{Cl}$), establishes alkali metal vacancies

as the predominant intrinsic charge carriers in bulk three-dimensional antiperovskite structures[36, 37].

Upon the introduction of defects, macroscopic ionic diffusion proceeds primarily via two distinct atomistic pathways. In the vacancy mechanism, alkali vacancies migrate via discrete hops along the edges of the X_6B octahedra. Although this mode is supported by a relatively high baseline concentration of intrinsic vacancy carriers, it is fundamentally limited by substantial migration energy barriers, typically calculated between 0.3 and 0.4 eV for pristine systems[28, 29]. Alternatively, interstitial-mediated transport offers a highly kinetically favorable pathway through the interstitial dumbbell mechanism. Rather than migrating as isolated point charges, an interstitial alkali ion coordinates with a lattice-site ion to form a split configuration centered at a single crystallographic vertex. Subsequent migration proceeds via a concerted, multi-ion knock-off process that dramatically reduces the structural energy barrier, frequently to values below 0.17 eV[38]. However, while their individual mobility is exceptional, the intrinsic equilibrium concentration of these interstitials remains negligible under ambient conditions due to their high formation energies[39, 40].

In antiperovskite solid electrolytes, macroscopic ionic conductivity is fundamentally governed by metal-halide Schottky pairs (e.g., LiCl Schottky defects), which dictate the material's dominant thermodynamic defect chemistry. First-principles computational studies consistently demonstrate that these metal-halide Schottky defects exhibit the lowest formation energies among all neutral defects, easily bypassing the intrinsically sparse populations of rapid, high-energy Frenkel interstitials[36, 37]. Furthermore, compared to the highly sluggish vacancies created by other intrinsic defects, such as Li_2O Schottky pairs, which remain tightly trapped by strong Coulombic attraction to the doubly charged oxygen vacancies, the alkali metal vacancies generated by metal-halide Schottky pairs exhibit uniquely weak binding energies to their host halide vacancies[28]. This highly favorable thermodynamic and kinetic landscape ensures that metal-halide Schottky pairs yield a higher equilibrium concentration of highly mobile, relatively untrapped alkali metal vacancies, establishing them as the primary charge carriers responsible for baseline ionic conductivity.

Despite this comparatively weak binding, the sheer abundance of these intrinsic vacancies introduces complex electrostatic interactions that still critically influence macroscopic transport kinetics. The stoichiometric formation of a metal-halide Schottky pair inherently necessitates the creation of an oppositely charged halide vacancy within the lattice[36]. In the solid-state matrix, the negatively charged alkali vacancy and the positively charged halide vacancy inevitably experience mutual Coulombic attraction[41]. While weaker than the severe attraction caused by oxygen vacancies, this electrostatic interplay still leads to the formation of localized defect pairs or clusters[42]. Consequently, while the total inventory of alkali vacancies is exceptionally high, a fraction of these potential carriers remains electrostatically tethered to the halide vacancies at ambient temperatures.

This residual trapping effect alters the effective potential energy surface for ion migration[36]. For an alkali vacancy to participate in long-range, macroscopic diffusion, it must overcome not only the intrinsic structural migration barrier along the octahedral edges but also

the defect binding energy required to fully dissociate from the localized Schottky pair[35]. If this binding energy is not sufficiently mitigated, the halide vacancy acts as a localized trap, attenuating the overall ionic conductivity despite the high absolute concentration of available charge carriers[43]. Therefore, investigating the precise atomistic configuration, binding energetics, and spatial influence of Schottky defect pairs constitutes a critical frontier in this research. By systematically isolating and analyzing these paired defects across varying antiperovskite compositions, it becomes possible to quantify their retarding effect on local migration pathways and, ultimately, to devise structural engineering strategies to further suppress defect trapping and fully unlock the superionic potential of the lattice.

2.4. Computational Modeling: DFT and CI-NEB

The quantum-mechanical description of a material's electronic structure begins with the time-independent Schrödinger equation, where the Hamiltonian accounts for the kinetic and potential energies of all interacting electrons and nuclei. Applying the Born–Oppenheimer approximation decouples nuclear and electronic motion, reducing the problem to electrons moving within a static ionic field[44, 45]. Even so, the many-electron wavefunction of an N-electron system depends on $3N$ spatial variables, causing memory requirements to scale exponentially with system size and rendering direct solution computationally intractable[46, 47].

Hohenberg and Kohn (1964) resolved this by proving that the ground-state electron density $\rho(\mathbf{r})$, which depends on only three spatial coordinates regardless of system size, uniquely determines the external potential and hence all ground-state properties[48]. Their second theorem establishes a variational principle: the true ground-state energy is obtained by minimizing the total energy functional $E[\rho]$ over all trial densities. Building on this, Kohn and Sham (1965) introduced an auxiliary system of non-interacting electrons reproducing the exact ground-state density of the true interacting system[49]. These electrons move in an effective Kohn–Sham potential comprising the external (nuclear), Hartree (classical electrostatic), and exchange–correlation contributions — the last of which captures all quantum many-body effects. The resulting single-particle equations are solved self-consistently: an initial density generates the potential, new orbitals are computed, and the density is updated iteratively until convergence.

Because the exact exchange–correlation functional is unknown, an approximation must be adopted[50]. The Generalized Gradient Approximation in the Perdew–Burke–Ernzerhof (GGA-PBE) form is the robust, well-validated standard for solid-state systems, accurately describing structural parameters, energetics, and electronic properties across a wide range of materials[51].

Coupling DFT with the climbing image nudged elastic band (CI-NEB) method enables the investigation of ion diffusion dynamics in crystalline solids, such as antiperovskite solid electrolytes[52]. The CI-NEB approach maps minimum-energy pathways to identify the transition states (saddle points) governing ion migration. This is achieved by generating a discretized path of structural images between an initial and final state via linear interpolation.

By optimizing these intermediate images using spring forces, the algorithm drives the highest-energy image to the saddle point, yielding a precise migration energy barrier[53].

Furthermore, the combination of DFT and CI-NEB provides critical insights into local atomic interactions, including defect binding energies and lattice distortions. Differential charge density analyses can determine the extent of Coulombic attraction between resulting vacancies. If a mobile vacancy is strongly bound to an oppositely charged defect, the binding energy effectively increases the overall activation energy required for macroscopic conduction. Additionally, NEB simulations highlight how subtle lattice adjustments, such as octahedral tilting or the widening of diffusion bottlenecks, can lower transition state energies.

2.5. Knowledge Gap and Motivation

While recent computational studies have provided valuable insights into the baseline ionic mobility of antiperovskite solid electrolytes, the majority of current research remains heavily focused on evaluating migration energies and diffusion pathways associated with isolated, single alkali point defects. However, as established by thermodynamic calculations, the formation energies for these single point defects are often prohibitively high, rendering their spontaneous concentration negligible under realistic ambient conditions. To accurately capture the macroscopic transport behavior of these materials, it is therefore imperative to model diffusion based on the thermodynamically dominant defect structures. Metal-halide Schottky defects, specifically LiCl/F and NaCl/F vacancy pairs, exhibit significantly lower formation energies and naturally generate a high abundance of mobile alkali vacancies (V'_{Li} and V'_{Na}). Consequently, investigating the atomistic behavior of these Schottky pairs is essential for understanding the true ionic conduction mechanisms in antiperovskite frameworks. Furthermore, while the prototypical Li_3OCl is widely studied, its practical, large-scale deployment faces significant macro-level challenges. Lithium is increasingly categorized as a critical raw material by the EU[54], and the industrial manufacturing of chlorine is highly energy-intensive[55]. These supply-chain and environmental vulnerabilities necessitate exploring alternative chemical spaces, specifically fluorine- and sulfur-substituted variants (Li_3OF, Li_3SCl). Crucially, this study expands its scope to include sodium-based families (Na_3OCl, Na_3OF, Na_3SCl) to provide a direct comparison with their lithium counterparts. This comparative approach is primarily motivated by the broader sustainability aspects of battery technologies, as sodium-based systems offer a much more abundant and environmentally benign alternative to conventional lithium-ion batteries[56, 57].

Utilizing first-principles calculations via Density Functional Theory as implemented in the Quantum ESPRESSO package, the primary objective is to evaluate the migration energy barriers of V'_{Li} and V'_{Na} within the immediate vicinity of these complex defect clusters. Specifically, this work aims to quantify how the localized lattice distortion induced by the introduction of the Schottky pair alters the surrounding potential energy surface. By correlating these structural perturbations with changes in the local migration barriers, this research seeks to uncover how realistic defect chemistries and their subsequent geometric deformations govern

the overall ionic conductivity. Ultimately, understanding these defect-driven mechanisms will inform the structural optimization and design of safer, high-performance solid-state batteries.

3. Methodology

All first-principles calculations were carried out using density functional theory (DFT) as implemented in the Quantum ESPRESSO package[58, 59]. The exchange-correlation energy was evaluated within the generalized gradient approximation (GGA) using the Perdew–Burke–Ernzerhof (PBE) functional[60], and electron-ion interactions were described using the projector augmented-wave (PAW) method[61]. For the structural models, 2 × 2 × 2 dimensions were utilized for both the primitive and defect supercells. The supercell size was tested and found to be sufficient (Figure 1). Prior to defect and migration evaluations, the lattice parameters for all compounds were subjected to strict convergence testing. A full variable-cell relaxation was executed to secure the equilibrium fixed lattice parameters before initiating the nudged elastic band (NEB) calculations[52]. Structural relaxations were performed with the total energy convergence in the self-consistent electronic loop set to $1.0 \times 10^{-8}\ eV$, and atomic positions were relaxed until the residual forces on all atoms were strictly less than $1.0 \times 10^{-3}\ eV/\text{Å}$. For the thermodynamic evaluation of defect formation energies, the Brillouin zone was sampled using a 3 × 3 × 3 Monkhorst-Pack k-point mesh[62]. Finally, ion migration energy barriers and pathways were simulated using the NEB method and subsequently refined with the climbing image nudged elastic band (CI-NEB) approach to accurately pinpoint the transition states[53]. A 2 × 2 × 2 k-point grid was utilized for all CI-NEB migration barrier calculations.

In modeling the defect chemistry, the construction of the initial and final states for the Schottky defect pair in Li_3OCl was guided by established theoretical approaches, wherein the lithium vacancy (V'_{Li}) and chlorine vacancy (V'_{Cl}) are positioned in close proximity. In these relatively rigid cubic structures, low-energy migration pathways are typically evaluated along the 100 family of crystallographic planes, such as the (001) plane[28]. However, applying this adjacent-vacancy assumption to softer, heavily distorted antiperovskite lattices, such as Li_3SCl and Na_3SCl, proved prohibitive. In these soft lattices, placing two vacancy sites immediately next to one another induces excessive local structural perturbation. Consequently, a systematic evaluation of various spatial configurations for the Schottky pairs was required. Multiple relative vacancy distances were tested, and only the arrangement exhibiting the lowest overall defect formation energy, representing the most thermodynamically stable state, was selected as the reference configuration.

DFT is also employed to evaluate the formation energies and thermodynamic stability of intrinsic defects. In antiperovskite systems like Li_3OCl, a LiCl Schottky defect comprises pairs of vacancies (e.g., V'_{Li} and $V^{\cdot}_{Cl}$). Defect formation energies are calculated by comparing the total energies of defective and pristine supercells, accounting for the chemical potentials of the constituent atoms. The formation energy was calculated using the following expression[37, 63, 64]:

$$E^{\mathrm{f}}[X] = E_{\mathrm{tot}}[X] - E_{\mathrm{tot}}[\mathrm{perfect}] - \sum_i n_i \mu_i$$

To quantify the degree of structural distortion within the local coordination environments, the Continuous Symmetry Measure (CSM) was employed[65]. The CSM serves as a quantitative measure of similarity, functioning as a "distance to a shape". A CSM value of 0.0 indicates a perfectly symmetric, undistorted ideal environment, with values increasing as the configuration becomes more distorted[66, 67]. Because the fundamental building block of the antiperovskite lattice is an electronically inverted octahedral framework, the actual, distorted local environment for a given site was specifically compared against an ideal octahedral model. Therefore, the calculated CSM value directly quantifies how closely the local lattice configuration resembles a perfect octahedron.

4. Results and Discussion

To ensure the numerical reliability and accuracy of the computational models, systematic convergence tests were conducted for all investigated compounds prior to the primary analysis. Figure 1 illustrates a representative example of this optimization process, displaying the total energy of the perfect Li_3OCl lattice evaluated across various Γ-centered k-point meshes. As the sampling density increases from a single Γ-point up to a $5 \times 5 \times 5$ grid, the total energy initially fluctuates before reaching a stable plateau, indicating that the Brillouin zone integration is sufficiently converged. Beyond k-point sampling, identical rigorous testing protocols were applied to evaluate other critical parameters, such as the energy cutoffs and lattice parameters, across all materials studied. This comprehensive approach guarantees that the derived energetic and structural properties are robust, computationally efficient, and independent of the chosen basis set size or reciprocal space sampling.

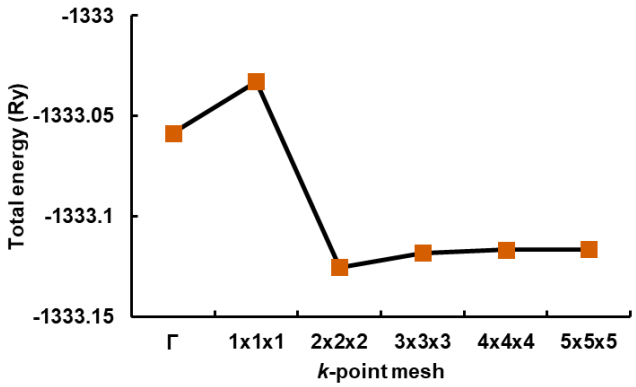

Figure 1. Convergence test of the total energy for the perfect lattice evaluated across various Γ-centered k-point meshes, from Γ-only to 5×5×5.

To validate the accuracy of the computational methodology, the calculated defect formation energies for the reference system were benchmarked against established literature values (Wu et al., 2018)[28]. As detailed in Table 1, the calculated energies for fundamental

defect configuration, including the LiCl and Li_2O Schottky defect pairs, Li_2O substitution by Cl, and the Frenkel defect pair, demonstrate strong alignment with previous models. The minor numerical deviations observed are expected standard variances within DFT calculations. These differences can be directly attributed to variations in computational boundary conditions, specifically the chosen supercell dimensions and the specific PBE pseudopotentials utilized in this study. Having established the numerical validity and reliability of this parameter set, the framework was confidently extended to evaluate the formation energies of the remaining metal-halide Schottky pairs across all six investigated antiperovskite compounds.

Table 1. Calculated defect formation energies (eV) in Li_3OCl compared to previously reported DFT values.

Defect types	Formation energy (eV)	Wu et al., 2018[28]
LiCl Schottky defect pair	1.39	1.27
Li_2O Schottky defect pair	1.59	1.54
Li_2O substitution by Cl	1.61	1.56
Frenkel defect pair	2.10	1.85

Extending the validated methodology, the formation energies of metal-halide Schottky defect pairs were calculated for the full series of six antiperovskite compounds. As detailed in Table 2, only Li_3OCl and Na_3OCl exhibit positive formation energies (1.391 eV and 1.027 eV, respectively), indicating thermodynamic stability under standard conditions. In stark contrast, the remaining four compounds (Li_3SCl, Li_3OF, Na_3SCl, and Na_3OF) yield substantially negative formation energies, ranging from -1.78 eV to -3.74 eV. These negative values dictate a strong spontaneous driving force for defect formation, indicative of pronounced intrinsic instability. This calculated thermodynamic instability correlates directly with the literature; according to Kim et al. (2022)[64], these specific unstable compounds exhibit remarkably high stabilization temperatures (exceeding 2100 K). The requirement of such extreme thermal energy to stabilize the lattice structures reflects their inherent low-temperature instability, perfectly aligning with the negative defect formation energies derived from our DFT calculations. To further elucidate the fundamental structural origins driving these thermodynamic instabilities, the CSM values for each compound are evaluated in the subsequent section (Figure 2).

Table 2. Calculated formation energy of metal-halides Schottky defect pair in 6 antiperovskite compounds.

Compounds	Formation energy (eV)
Li_3OCl	1.39
Li_3SCl	-2.69
Li_3OF	-2.15
Na_3OCl	1.03
Na_3SCl	-1.78
Na_3OF	-3.74

To elucidate the fundamental structural origins driving the observed thermodynamic instabilities, CSM were evaluated for the initial relaxed states of all six antiperovskite compounds. As depicted in Figure 2, a direct correlation emerges between the degree of structural distortion and the previously calculated defect formation energies. The thermodynamically stable compounds, Li_3OCl and Na_3OCl, exhibit minimal CSM values (0.27 and 0.22, respectively), indicating that their atomic arrangements closely adhere to the ideal, highly symmetric cubic antiperovskite lattice. In sharp contrast, the four compounds that yielded negative formation energies display significantly elevated CSM values. The sulfur-substituted structures, Li_3SCl and Na_3SCl, exhibit the most severe structural distortions with CSM values approaching 1.99 and 1.80, while the fluoride-based compounds (Li_3OF and Na_3OF) demonstrate moderate but still substantial symmetry breaking. This quantification confirms that the thermodynamically unstable compounds suffer from a large degree of intrinsic lattice distortion. Physically, this geometric deviation from the ideal polyhedral coordination generates severe internal strain, likely arising from ionic size mismatches and steric hindrance between the specific alkali metals, chalcogens, and halogens. The accumulation of this internal elastic energy destabilizes the lattice, ultimately providing the system's strong driving force for phase decomposition rather than maintaining the heavily strained antiperovskite configuration.

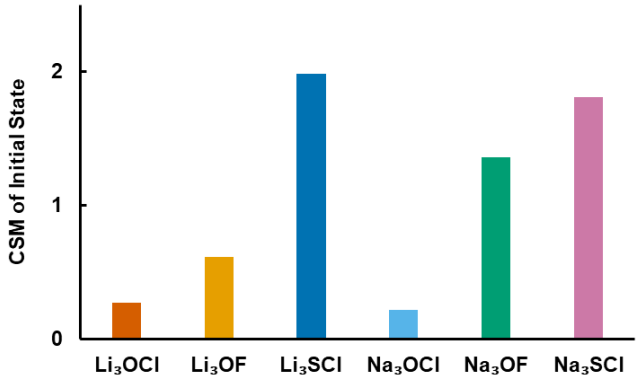

Figure 2. CSM of initial state for 6 antiperovskite compounds.

Following the thermodynamic and initial structural assessments, the ionic transport properties of the antiperovskite compounds were evaluated by calculating the migration barriers for the respective alkali ions. As summarized in Table 3, the activation energies exhibit significant sensitivity to the specific anionic composition. Within the lithium-based systems, the reference Li_3OCl compound presents the highest migration barrier at 0.34 eV. Chemical substitution substantially enhances the theoretical transport kinetics; introducing fluorine (Li_3OF) or sulfur (Li_3SCl) reduces the barriers to 0.21 eV and 0.22 eV, respectively. A related, though distinct, trend is observed in the sodium-based analogues. The baseline Na_3OCl exhibits a migration barrier of 0.310 eV, which similarly drops to 0.21 eV upon fluoride substitution (Na_3OF). Conversely, sulfur substitution in the sodium system (Na_3SCl) results in a slight increase in the barrier to 0.336 eV. To understand the fundamental structural mechanics driving these numerical variations, the migration energy profiles were analyzed in conjunction with dynamic lattice distortions. In the subsequent section, the calculated migration barriers are plotted alongside their corresponding CSM values as a function of the ionic migration path (Figure 3)

Table 3. Calculated metal-halide Schottky pairs migration barriers (eV) for Li- and Na-based antiperovskite compounds.

Li-compounds	Migration Barrier (eV)	Na-compounds	Migration Barrier (eV)
Li_3OCl	0.34	Na_3OCl	0.31
Li_3OF	0.21	Na_3OF	0.21
Li_3SCl	0.22	Na_3SCl	0.34

Figure 3 presents the calculated migration energy profiles alongside the corresponding CSM evolutions along the reaction path for the lithium-based antiperovskites (Li_3OCl, Li_3OF, and Li_3SCl). As observed in the left column, the energy barriers vary depending on the anionic composition, with Li_3OCl exhibiting the highest peak barrier at 0.34 eV, while the substituted

Li_3OF and Li_3SCl compounds show reduced maximum barriers of 0.21 eV and 0.22 eV, respectively. Additionally, the total distance of the reaction coordinates varies across the compounds, extending from 5.72 Å in Li_3OCl to 8.60 Å in Li_3SCl; this variation is expected, as the larger the cell is, the longer the migration path should be.

To understand the structural dynamics facilitating this transport, the CSM values were evaluated along the same reaction paths (Figure 3, right column). For a lithium vacancy to move to an adjacent site, the surrounding lattice must undergo localized distortion to open the transport bottleneck. This geometric accommodation is clearly captured by the CSM profiles, where the peaks in symmetry breaking align with the transition states of the migration barriers. Furthermore, a comparative analysis of the numerical CSM values reveals an inverse relationship between the degree of distortion and the activation energy: a higher maximum CSM value corresponds to a lower migration barrier. The baseline Li_3OCl exhibits a relatively rigid transport mechanism with a peak CSM at 0.97, resulting in the highest energy penalty. In contrast, the highly distorted transient states of Li_3OF and Li_3SCl reach peak CSM values at 1.94 and 2.81, respectively. This indicates that a greater structural flexibility—manifested as a larger capacity for transient symmetry breaking—effectively softens the transport bottleneck, thereby lowering the overall migration barrier and facilitating more efficient ionic conduction.

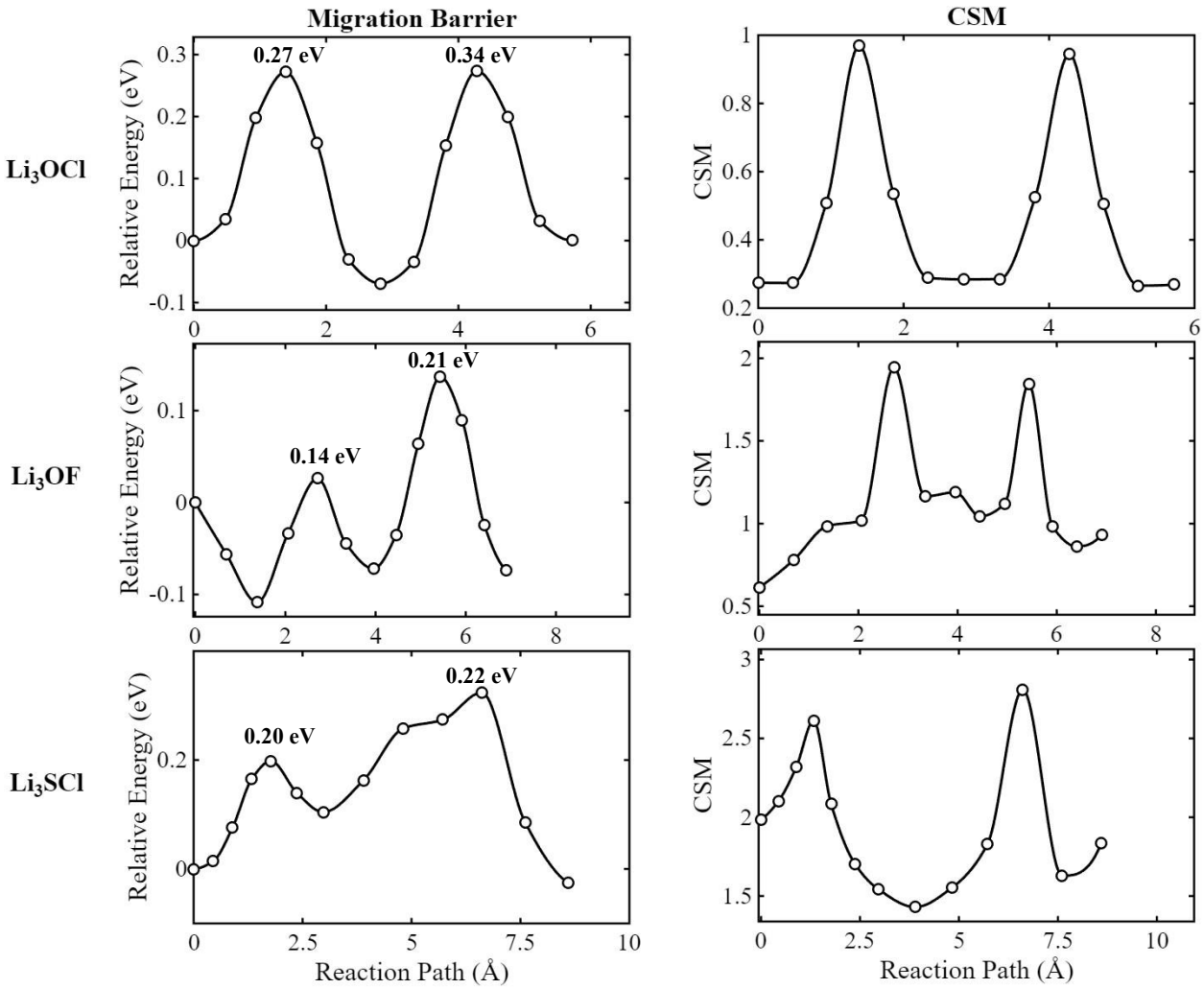

Figure 3. NEB migration barrier profiles (left) and continuous symmetry measure (CSM) along the reaction path (right) for Li-ion migration in Li_3OCl, Li_3OF, and Li_3SCl. Annotated values indicate the forward migration barriers at each transition state.

Turning to the sodium-based antiperovskites, Figure 4 illustrates the migration energy profiles and corresponding CSM evolutions for Na_3OCl, Na_3OF, and Na_3SCl. Broadly, the fundamental transport mechanism remains consistent with that of the lithium analogues: localized lattice distortions, quantified by the CSM peaks, aligning with the transition states to facilitate ionic movement. This inverse relationship holds true for the fluoride-substituted Na_3OF, where substantial transient symmetry breaking (peak CSM = 2.58) successfully suppresses the maximum migration barrier to 0.21 eV, an improvement over the 0.310 eV baseline of Na_3OCl. However, Na_3SCl presents a notable deviation from this established trend. Despite exhibiting a highly flexible, distorted transient state (peak CSM = 2.70), its maximum activation energy paradoxically increases to 0.34 eV. To understand this numerical anomaly, the physical distance of the transport route must be considered. As evident from the reaction coordinates, the total migration path for Na_3SCl extends to 10.98 Å—considerably longer than the 8.70 Å paths of its counterparts—driven by the substantial supercell expansion required to

accommodate both the larger sodium and sulfur ions. This observation aligns with recent predictive modeling; a machine learning analysis by Kim et al. (2022)[64] evaluating the relative importance of various structural properties in alkali ion transport concluded that the migration path length is the most dominant factor governing activation energy. Therefore, in the case of Na_3SCl, the severe kinetic penalty imposed by navigating this extensively elongated transport distance effectively overwhelms the energetic benefits provided by the lattice flexibility, ultimately resulting in an elevated overall migration barrier.

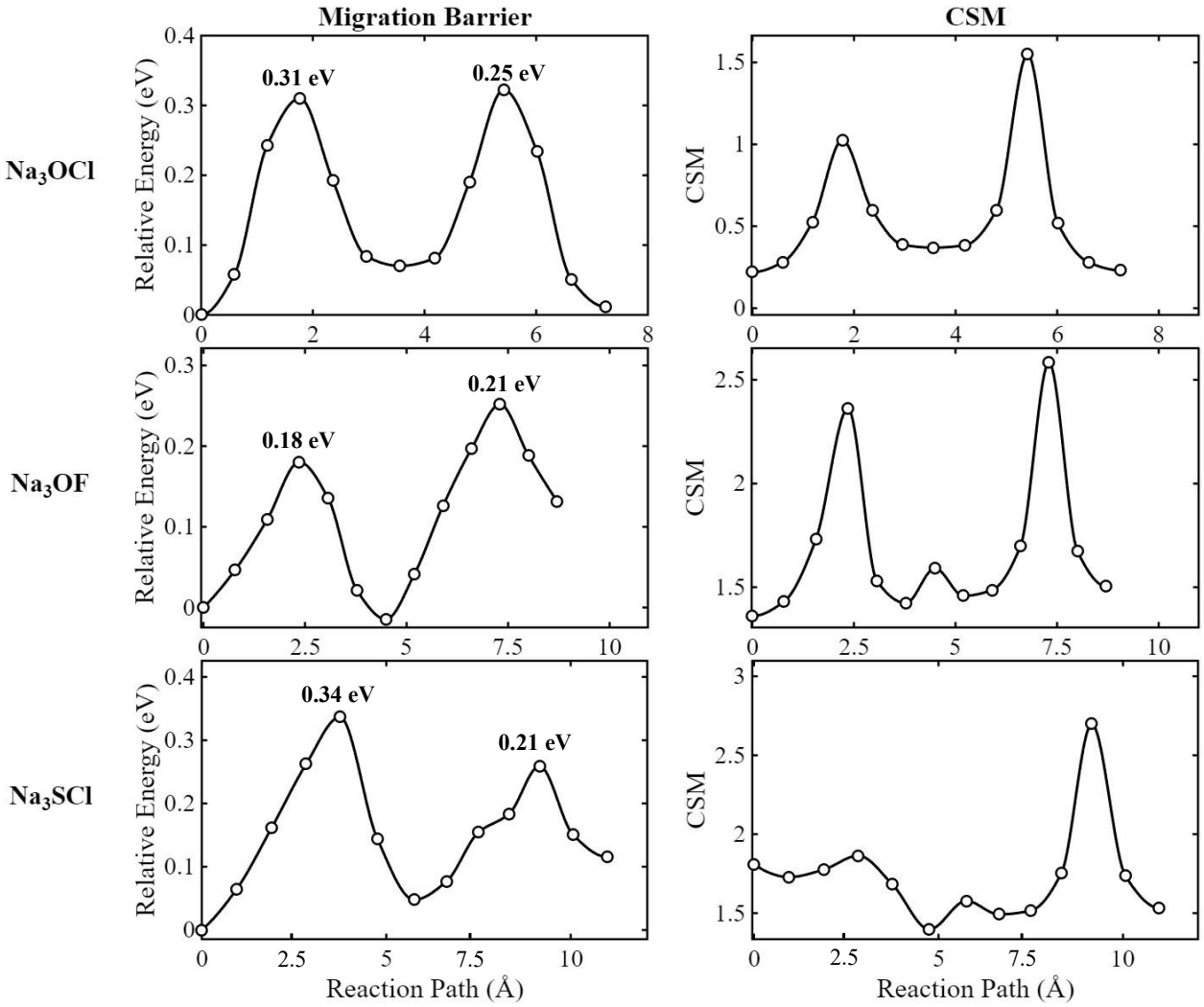

Figure 4. NEB migration barrier profiles (left) and continuous symmetry measure (CSM) along the reaction path (right) for Na-ion migration in Na_3OCl, Na_3OF, and Na_3SCl. Annotated values indicate the forward migration barriers at each transition state.

Figure 5 synthesizes the overarching relationship between transient structural distortion, quantified by the corresponding CSM, and the resulting migration energy barriers across the evaluated antiperovskite systems. As illustrated by the general trendline, a distinct inverse correlation is established: an increased degree of transient lattice distortion broadly corresponds to a reduction in the migration barrier. This structural mechanism indicates that heightened

lattice flexibility effectively lowers the kinetic energy required for ionic transport. However, this kinetic advantage is inherently coupled with a critical thermodynamic vulnerability. As established in the preceding thermodynamic evaluations, the compounds exhibiting the highest distortion and lowest barriers—specifically Li_3OF, Li_3SCl, Na_3OF, and Na_3SCl—are intrinsically unstable, characterized by negative defect formation energies and a strong driving force for decomposition. Consequently, these findings highlight a fundamental paradigm in solid-state electrolyte engineering. The rational design of next-generation electrolytes cannot focus exclusively on minimizing migration barriers to maximize ionic mobility; it must simultaneously satisfy stringent thermodynamic stability criteria. Ultimately, successful material engineering requires striking a delicate, optimized balance: inducing sufficient local structural flexibility to facilitate rapid ion migration while maintaining the robust structural integrity required to prevent spontaneous phase degradation under standard operating conditions.

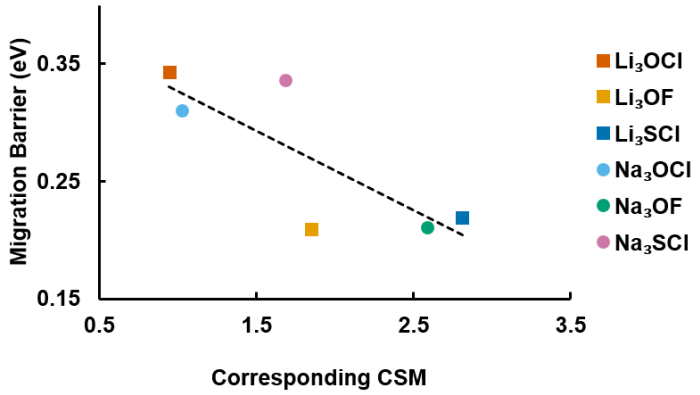

Figure 5. Correlation between the continuous symmetry measure (CSM) at the migration peak and the corresponding migration energy barrier for 6 antiperovskite compounds.

4.1. Sustainability

This study's contribution to sustainability lies primarily in reducing the experimental burden associated with screening antiperovskite solid electrolytes, since all evaluations were performed computationally via DFT and CI-NEB rather than through hazardous synthesis and testing of hygroscopic, air-sensitive lithium and sodium compounds. By identifying that fluoride-substituted compositions (Li_3OF, Na_3OF) achieve the lowest migration barriers while sodium-based compounds perform comparably to their lithium counterparts, the work provides concrete evidence that sodium chemistries—built on a far more abundant and less geopolitically constrained element than lithium, which the EU classifies as a critical raw material—can serve as viable substitutes without sacrificing ionic transport performance.

Looking beyond the immediate results, the geometric design principles established here, linking CSM to migration barrier reduction, could substantially accelerate the discovery of

next-generation solid electrolytes while cutting down the trial-and-error experimentation that typically consumes significant energy, solvents, and rare materials in battery R&D. Wider deployment of antiperovskite-based all-solid-state batteries guided by these principles could displace flammable liquid electrolytes and graphite anodes, lowering thermal-runaway risk in consumer electronics, electric vehicles, and grid storage, and thereby supporting global decarbonization goals tied to renewable energy integration. Realizing this potential responsibly will require follow-up work on scalable, low-toxicity synthesis routes and lifecycle assessments to ensure that any efficiency gains in ionic conductivity are not offset by unforeseen environmental or supply-chain costs during industrial scale-up.

5. Conclusion

This study systematically investigated the influence of metal-halide Schottky defect pairs on ionic transport across six antiperovskite solid electrolyte compounds — Li_3OCl, Li_3SCl, Li_3OF, Na_3OCl, Na_3SCl, and Na_3OF — using first-principles Density Functional Theory (DFT) and the climbing image nudged elastic band (CI-NEB) method. The results establish a clear and consistent mechanistic picture of defect-driven ionic conduction in these materials.

Thermodynamic analysis revealed that only Li_3OCl and Na_3OCl exhibit positive Schottky defect formation energies, indicating intrinsic stability under ambient conditions, while the remaining four compounds display strongly negative formation energies associated with pronounced lattice instability. This instability was directly correlated with elevated Continuous Symmetry Measure (CSM) values, confirming that compounds deviating most from ideal octahedral symmetry are thermodynamically prone to phase decomposition. Despite this vulnerability, the same structural flexibility that destabilizes these lattices proves kinetically advantageous: fluoride-substituted compounds Li_3OF and Na_3OF yielded the lowest migration barriers of 0.21 eV for both systems, driven by their capacity for transient symmetry breaking at the transition state. Conversely, Na_3SCl, despite exhibiting high lattice flexibility (peak CSM = 2.70), suffers from an elongated migration path of 10.98 Å, demonstrating that migration path distance can override the benefits of lattice softness and become the dominant factor governing activation energy.

A key finding of this work is the inverse correlation between the peak CSM at the transition state and the migration energy barrier across all six compounds. This geometric design principle — that greater localized lattice distortion fundamentally lowers the kinetic barrier — provides a quantitative structural descriptor that can guide the rational engineering of next-generation antiperovskite electrolytes. Practically, this implies that compositional strategies targeting moderate, controlled lattice flexibility, without sacrificing thermodynamic stability, represent the most promising avenue for optimizing ionic conductivity.

Ultimately, this research demonstrates that the rational design of antiperovskite solid electrolytes must balance two competing requirements: sufficient local structural flexibility to lower migration barriers and enable fast ionic transport, and adequate thermodynamic stability

to prevent spontaneous phase decomposition under operating conditions. The geometric design principles derived from this study — particularly the predictive power of the transition-state CSM as a descriptor for ionic mobility — provide a practical and computationally accessible framework for accelerating the discovery and optimization of safe, high-performance solid electrolytes for next-generation all-solid-state batteries.

6. Future Work

It is worth noting that this work focuses exclusively on monovalent alkali-ion conductors, specifically Li^+- and Na^+-based antiperovskite frameworks. Aluminum-based systems, which involve Al^{3+} charge carriers, belong to the distinct category of multivalent-ion batteries; the substantially higher ionic charge of Al^{3+} introduces fundamentally different electrostatic interactions, defect formation mechanisms, and transport physics. Extending the present computational framework to multivalent antiperovskite or related solid electrolytes therefore represents a promising direction for future work, warranting a separate, dedicated investigation.

A second avenue for future work concerns experimental validation of the computed migration barriers. Directly resolving defect-scale ionic migration pathways in solid electrolytes remains experimentally challenging; although techniques such as neutron diffraction, nuclear magnetic resonance (NMR), and muon spin spectroscopy have been used to probe ion transport, they still lack the spatial precision needed to isolate individual defect-driven pathways. Consequently, rather than substituting for experimental validation, this computational study is best positioned as a high-throughput screening framework: by identifying the structural and geometric descriptors that govern ionic transport, it proposes candidate compositions and design principles that can guide future targeted synthesis and characterization efforts. Future work should therefore prioritize experimental collaboration to synthesize the most promising candidates identified here—particularly the fluoride-substituted compositions—and apply advanced characterization techniques to test the geometric design principles proposed, stimulating further experimental and theoretical investigation within the ionic solid research field.

Declaration of Generative AI in the Writing Process

During the preparation of this work, the author used Gemini 3.0 Pro to refine the phrasing and check for grammatical errors in the thesis. After using this tool, the author reviewed and edited the content as needed and takes full responsibility for the content of the publication.

References

[1] G. Yang, D. Zha, D. Cao, and G. Zhang, "Time for a change: Rethinking the global renewable energy transition from the Sustainable Development Goals and the Paris Climate Agreement," *The Innovation,* vol. 5, no. 2, 2024.

[2] A. J. Gabric, "The climate change crisis: a review of its causes and possible responses," *Atmosphere,* vol. 14, no. 7, p. 1081, 2023.

[3] A. V. Olympios *et al.*, "Progress and prospects of thermo-mechanical energy storage—a critical review," *Progress in Energy,* vol. 3, no. 2, p. 022001, 2021.

[4] P. K. Dubey, B. Singh, D. Singh, P. N. Verma, and K. Verma, "Energy Storage Technologies: Types, Recent Trends, and Development," in *2024 3rd International conference on Power Electronics and IoT Applications in Renewable Energy and its Control (PARC)*, 2024: IEEE, pp. 1-7.

[5] S. J. Osibodu, A. M. Adeyinka, and O. V. Mbelu, "Phase change material integration in concrete for thermal energy storage: techniques and applications in sustainable building," *Sustainable Energy Research,* vol. 11, no. 1, p. 45, 2024.

[6] M. I. Khan, R. Gilani, J. Hafeez, R. Ayoub, I. Zahoor, and G. Saira, "Advantages and disadvantages of lithium-ion batteries," in *Nanostructured Lithium-ion Battery Materials*: Elsevier, 2025, pp. 47-64.

[7] D. Wu and F. Wu, "Toward better batteries: Solid-state battery roadmap 2035+," *Etransportation,* vol. 16, p. 100224, 2023.

[8] X. Yu, R. Chen, L. Gan, H. Li, and L. Chen, "Battery safety: From lithium-ion to solid-state batteries," *Engineering,* vol. 21, pp. 9-14, 2023.

[9] F. Zheng, M. Kotobuki, S. Song, M. O. Lai, and L. Lu, "Review on solid electrolytes for all-solid-state lithium-ion batteries," *Journal of Power Sources,* vol. 389, pp. 198-213, 2018.

[10] C. Chen, S. Xie, E. Sperling, A. Yang, G. Henriksen, and K. Amine, "Stable lithium-ion conducting perovskite lithium–strontium–tantalum–zirconium–oxide system," *Solid State Ionics,* vol. 167, no. 3-4, pp. 263-272, 2004.

[11] D. Zhang *et al.*, "Research progress and application of PEO-based solid state polymer composite electrolytes," *Frontiers in Energy Research,* vol. 9, p. 726738, 2021.

[12] A. R. Polu *et al.*, "Impact of tetracyanoethylene plasticizer on PEO based solid polymer electrolytes for improved ionic conductivity and solid-state lithium-ion battery performance," *Journal of Power Sources,* vol. 625, p. 235742, 2025.

[13] M. Zhang *et al.*, "Advanced High-Voltage Electrolyte Design Using Poly (ethylene Oxide) and High-Concentration Ionic Liquids for All-Solid-State Lithium-Metal Batteries," *ACS Applied Materials & Interfaces,* vol. 16, no. 41, pp. 56095-56105, 2024.

[14] A. Machín, F. Díaz, M. C. Cotto, J. Ducongé, and F. Márquez, "Recent advances in dendrite suppression strategies for solid-state lithium batteries: From interface engineering to material innovations," *Batteries,* vol. 11, no. 8, p. 304, 2025.

[15] J. Feng, Z. Gao, L. Sheng, Z. Hao, and F. R. Wang, "Progress and perspective of interface design in garnet electrolyte-based all-solid-state batteries," *Carbon Energy,* vol. 3, no. 3, pp. 385-409, 2021.

[16] S. K. Choi, J. Han, G. J. Kim, Y. H. Kim, J. Choi, and M. Yang, "A review of inorganic solid electrolytes for all-solid-state lithium batteries: Challenges and progress," *Journal of Powder Materials,* vol. 31, no. 4, pp. 293-301, 2024.

[17] M. D. Bouguern, N. G. Ningappa, K. Vishweswariah, A. Kumar MR, R. Kanno, and K. Zaghib, "Comparative Advances in Sulfide and Halide Electrolytes for Commercialization of All-Solid-State Lithium Batteries," *Advanced Materials,* vol. 38, no. 2, p. e13255, 2026.
[18] H. Su *et al.*, "Recent progress of sulfide electrolytes for all-solid-state lithium batteries," *Energy Materials,* vol. 2, no. 1, pp. N/A-N/A, 2022.
[19] M. Liu *et al.*, "Surface molecular engineering to enable processing of sulfide solid electrolytes in humid ambient air," *Nature Communications,* vol. 16, no. 1, p. 213, 2025.
[20] J. Liang *et al.*, "Current status and future directions in environmental stability of sulfide solid-state electrolytes for all-solid-state batteries," *Energy Material Advances,* vol. 4, p. 0021, 2023.
[21] R. Schlem, A. Banik, M. Eckardt, M. Zobel, and W. G. Zeier, "Na3–x Er1–x Zr x Cl6—A halide-based fast sodium-ion conductor with vacancy-driven ionic transport," *ACS Applied Energy Materials,* vol. 3, no. 10, pp. 10164-10173, 2020.
[22] R. Xu *et al.*, "Halide solid electrolytes in all-solid-state batteries: Ion transport kinetics, failure mechanisms and improvement strategies," *Nano Energy,* vol. 132, p. 110435, 2024.
[23] Y. Zhao and L. L. Daemen, "Superionic conductivity in lithium-rich anti-perovskites," *Journal of the American Chemical Society,* vol. 134, no. 36, pp. 15042-15047, 2012.
[24] X. Lü *et al.*, "Li-rich anti-perovskite Li 3 OCl films with enhanced ionic conductivity," *Chemical communications,* vol. 50, no. 78, pp. 11520-11522, 2014.
[25] M. J. Clarke, J. A. Dawson, T. J. Mays, and M. S. Islam, "Atomistic insights into the effects of doping and vacancy clustering on Li-ion conduction in the Li3OCl antiperovskite solid electrolyte," *ACS Applied Energy Materials,* vol. 4, no. 5, pp. 5094-5100, 2021.
[26] C. Guan *et al.*, "Unlocking the chemical space in anti-perovskite conductors by incorporating anion rotation dynamics," *Energy Storage Materials,* vol. 62, p. 102936, 2023.
[27] S. Gao *et al.*, "Hydride-based antiperovskites with soft anionic sublattices as fast alkali ionic conductors," *Nature communications,* vol. 12, no. 1, p. 201, 2021.
[28] M. Wu, B. Xu, X. Lei, K. Huang, and C. Ouyang, "Bulk properties and transport mechanisms of a solid state antiperovskite Li-ion conductor Li 3 OCl: insights from first principles calculations," *Journal of Materials Chemistry A,* vol. 6, no. 3, pp. 1150-1160, 2018.
[29] Y. Zhang, Y. Zhao, and C. Chen, "Ab initio study of the stabilities of and mechanism of superionic transport in lithium-rich antiperovskites," *Physical Review B—Condensed Matter and Materials Physics,* vol. 87, no. 13, p. 134303, 2013.
[30] W. Feng, L. Zhu, X. Dong, Y. Wang, Y. Xia, and F. Wang, "Enhanced Moisture Stability of Lithium-Rich Antiperovskites for Sustainable All-Solid-State Lithium Batteries," *Advanced Materials,* vol. 35, no. 12, p. 2210365, 2023.
[31] Y. Li *et al.*, "Fluorine-doped antiperovskite electrolyte for all-solid-state lithium-ion batteries," *Angewandte Chemie,* vol. 128, no. 34, pp. 10119-10122, 2016.
[32] B. A. Williamson, K. Eggestad, and S. M. Selbach, "Pseudo-lithium vacancies in hydrogen rich Li 3 OCl," *Journal of Materials Chemistry A,* vol. 13, no. 12, pp. 8816-8824, 2025.

[33] C. Li, S. Lian, C. Kang, J. Ren, and M. Chen, "Insights on transport performance, thermodynamic properties, and mechanical properties of Ruddlesden–Popper antiperovskite LiBr (Li2OHBr) 2 and LiBr (Li3OBr) 2," *The Journal of Chemical Physics,* vol. 159, no. 2, 2023.
[34] J. A. Dawson, P. Canepa, T. Famprikis, C. Masquelier, and M. S. Islam, "Atomic-scale influence of grain boundaries on Li-ion conduction in solid electrolytes for all-solid-state batteries," *Journal of the American Chemical Society,* vol. 140, no. 1, pp. 362-368, 2018.
[35] M.-H. Chen, A. Emly, and A. Van der Ven, "Anharmonicity and phase stability of antiperovskite Li 3 OCl," *Physical Review B,* vol. 91, no. 21, p. 214306, 2015.
[36] Z. Lu, C. Chen, Z. M. Baiyee, X. Chen, C. Niu, and F. Ciucci, "Defect chemistry and lithium transport in Li 3 OCl anti-perovskite superionic conductors," *Physical Chemistry Chemical Physics,* vol. 17, no. 48, pp. 32547-32555, 2015.
[37] A. C. C. Dutra, G. E. Rudman, K. E. Johnston, and J. A. Dawson, "Defect chemistry and ion transport in low-dimensional-networked Li-rich anti-perovskites as solid electrolytes for solid-state batteries," *Energy Advances,* vol. 2, no. 5, pp. 653-666, 2023.
[38] A. Emly, E. Kioupakis, and A. Van der Ven, "Phase stability and transport mechanisms in antiperovskite Li3OCl and Li3OBr superionic conductors," *Chemistry of Materials,* vol. 25, no. 23, pp. 4663-4670, 2013.
[39] P. Li, F. Hussain, P. Cui, Z. Li, and J. Yang, "Boosting ionic conductivity in antiperovskite Li 3 OCl via defect engineering: Interstitial versus vacancy," *Physical Review Materials,* vol. 3, no. 11, p. 115402, 2019.
[40] X. Luo, Y. Li, and X. Zhao, "Theoretical design of defects as a driving force for ion transport in Li3OBr solid electrolyte," *Energy & Environmental Materials,* vol. 7, no. 3, p. e12627, 2024.
[41] K. Rao and C. Rao, "Schottky Defects in Alkali Halides: Their Creation, Interaction, and Migration," *physica status solidi (b),* vol. 28, no. 1, pp. 157-169, 1968.
[42] B. A. Goldmann, M. J. Clarke, J. A. Dawson, and M. S. Islam, "Atomic-scale investigation of cation doping and defect clustering in the anti-perovskite Na 3 OCl sodium-ion conductor," *Journal of Materials Chemistry A,* vol. 10, no. 5, pp. 2249-2255, 2022.
[43] L. Xia, K. Zhang, and Y. Pei, "Unraveling defect-mediated ion transport behavior in anti-perovskite solid-state electrolytes via machine learning molecular dynamics simulations," *Physical Chemistry Chemical Physics,* vol. 28, no. 17, pp. 10698-10707, 2026.
[44] G. Panati, H. Spohn, and S. Teufel, "The time-dependent Born-Oppenheimer approximation," *ESAIM: Mathematical Modelling and Numerical Analysis,* vol. 41, no. 2, pp. 297-314, 2007.
[45] J. S. Briggs and J. M. Rost, "Time dependence in quantum mechanics," *The European Physical Journal D-Atomic, Molecular, Optical and Plasma Physics,* vol. 10, no. 3, pp. 311-318, 2000.
[46] U. Röthlisberger, "Introduction to electronic structure methods," *EPFL, Lausanne,* 2015.
[47] H. G. Burton, D. Marti-Dafcik, D. P. Tew, and D. J. Wales, "Exact electronic states with shallow quantum circuits from global optimisation," *npj Quantum Information,* vol. 9, no. 1, p. 75, 2023.

[48] P. Hohenberg and W. Kohn, "Inhomogeneous electron gas," *Physical review,* vol. 136, no. 3B, p. B864, 1964.
[49] W. Kohn and L. J. Sham, "Self-consistent equations including exchange and correlation effects," *Physical review,* vol. 140, no. 4A, p. A1133, 1965.
[50] A. D. Becke, "Perspective: Fifty years of density-functional theory in chemical physics," *The Journal of chemical physics,* vol. 140, no. 18, 2014.
[51] P. Haas, F. Tran, P. Blaha, K. Schwarz, and R. Laskowski, "Insight into the performance of GGA functionals for solid-state calculations," *Physical Review B—Condensed Matter and Materials Physics,* vol. 80, no. 19, p. 195109, 2009.
[52] H. Jónsson, G. Mills, and K. W. Jacobsen, "Nudged elastic band method for finding minimum energy paths of transitions," in *Classical and quantum dynamics in condensed phase simulations*: World Scientific, 1998, pp. 385-404.
[53] G. Henkelman, B. P. Uberuaga, and H. Jónsson, "A climbing image nudged elastic band method for finding saddle points and minimum energy paths," *The Journal of chemical physics,* vol. 113, no. 22, pp. 9901-9904, 2000.
[54] E. Commission, "Critical Raw Materials Resilience: Charting a Path towards greater Security and Sustainability," European Commission, Brussels, COM(2020) 474 final, 2020. Accessed: 1 July 2026. [Online]. Available: https://eur-lex.europa.eu/legal-content/EN/TXT/?uri=CELEX:52020DC0474
[55] K. Li, Q. Fan, H. Chuai, H. Liu, S. Zhang, and X. Ma, "Revisiting chlor-alkali electrolyzers: from materials to devices," *Transactions of Tianjin University,* vol. 27, no. 3, pp. 202-216, 2021.
[56] Z. Xu and J. Wang, "Toward emerging sodium-based energy storage technologies: from performance to sustainability," *Advanced Energy Materials,* vol. 12, no. 29, p. 2201692, 2022.
[57] A. N. Singh *et al.*, "Unleashing the potential of sodium-ion batteries: current state and future directions for sustainable energy storage," *Advanced Functional Materials,* vol. 33, no. 46, p. 2304617, 2023.
[58] P. Giannozzi *et al.*, "Advanced capabilities for materials modelling with Quantum ESPRESSO," *Journal of physics: Condensed matter,* vol. 29, no. 46, p. 465901, 2017.
[59] P. Giannozzi *et al.*, "QUANTUM ESPRESSO: a modular and open-source software project for quantum simulations of materials," *Journal of physics: Condensed matter,* vol. 21, no. 39, p. 395502, 2009.
[60] J. P. Perdew, K. Burke, and M. Ernzerhof, "Generalized gradient approximation made simple," *Physical review letters,* vol. 77, no. 18, p. 3865, 1996.
[61] P. E. Blöchl, "Projector augmented-wave method," *Physical review B,* vol. 50, no. 24, p. 17953, 1994.
[62] H. J. Monkhorst and J. D. Pack, "Special points for Brillouin-zone integrations," *Physical review B,* vol. 13, no. 12, p. 5188, 1976.
[63] C. G. Van de Walle and J. Neugebauer, "First-principles calculations for defects and impurities: Applications to III-nitrides," *Journal of applied physics,* vol. 95, no. 8, pp. 3851-3879, 2004.
[64] K. Kim *et al.*, "Exploring the synthesis of alkali metal anti-perovskites," *Chemistry of Materials,* vol. 34, no. 3, pp. 947-958, 2022.
[65] M. Pinsky and D. Avnir, "Continuous symmetry measures. 5. The classical polyhedra," *Inorganic chemistry,* vol. 37, no. 21, pp. 5575-5582, 1998.

[66] R. Chen, Z. Xu, Y. Lin, B. Lv, S.-H. Bo, and H. Zhu, "Influence of structural distortion and lattice dynamics on li-ion diffusion in li3ocl1–x br x superionic conductors," *ACS Applied Energy Materials,* vol. 4, no. 3, pp. 2107-2114, 2021.
[67] D. Waroquiers *et al.*, "Statistical analysis of coordination environments in oxides," *Chemistry of Materials,* vol. 29, no. 19, pp. 8346-8360, 2017.